The intra-seasonal dynamics of the mixed layer pump in the subpolar North Atlantic Ocean: a BGC-Argo float approach

L. Lacour, N. Briggs, Hervé Claustre, M. Ardyna, G. Dall'Olmo

The intra-seasonal dynamics of the mixed layer pump in the subpolar North Atlantic Ocean: a BGC-Argo float approach.

L. Lacour[1]†, N. Briggs[2], H. Claustre[1], M. Ardyna[1,3], G. Dall'Olmo[4,5]

[1]Sorbonne Université, CNRS, Laboratoire d'Océanographie de Villefranche, LOV, F-06230 Villefranche-sur-mer, France.

[2]National Oceanography Centre, European Way, Southampton SO14 3ZH, UK.

[3]Department of Earth System Science, Stanford University, Stanford CA 94305, USA.

[4]Plymouth Marine Laboratory, Prospect Place, The Hoe, Plymouth PL1 3DH, UK.

[5]National Centre for Earth Observation, Plymouth Marine Laboratory, Prospect Place, The Hoe, Plymouth PL1 3DH, UK.

Corresponding author: Léo Lacour (leo.lacour@takuvik.ulaval.ca)

† Now at Takuvik Joint International Laboratory, CNRS and Université Laval, Québec, G1V0A6, Canada.

Key Points:

- The density of BGC-Argo float network enables identification of episodic mixed layer pump events on a basin-scale.
- Intra-seasonal dynamics of the mixed layer pump drives episodic inputs of fresh organic material to the mesopelagic during the winter to spring transition.
- This mechanism provides a significant source of energy to the mesopelagic food-web before the spring bloom period.

Abstract

The detrainment of organic matter from the mixed layer, a process known as the mixed layer pump (ML pump), has long been overlooked in carbon export budgets. Recently, the ML pump has been investigated at seasonal scale and appeared to contribute significantly to particulate organic carbon export to the mesopelagic zone, especially at high latitudes where seasonal variations of the mixed layer depth are large. However, the dynamics of the ML pump at intra-seasonal scales remains poorly known, mainly because the lack of observational tools suited to

studying such dynamics. In the present study, using a dense network of autonomous profiling floats equipped with bio-optical sensors, we captured widespread episodic ML pump-driven export events, during the winter and early spring period, in a large part of the subpolar North Atlantic Ocean. The intra-seasonal dynamic of the ML pump exports fresh organic material to depth (basin-scale average up to 55 mg C m^{-2} d^{-1}), providing a significant source of energy to the mesopelagic food web before the spring bloom period. This mechanism may sustain the seasonal development of overwintering organisms such as copepods with potential impact on the characteristics of the forthcoming spring phytoplankton bloom through predator-prey interactions.

1 Introduction

The export of organic matter from the surface to the ocean interior has traditionally been attributed to the gravitational settling of particulate organic carbon (POC), namely the biological gravitational pump (Sanders et al., 2014; Siegel et al., 2016). The gravitational pump at high latitudes is closely related to the spring phytoplankton bloom (Martin et al., 2011). Large phytoplankton cells such as diatoms (> 20 µm) that thrive during the spring bloom contribute significantly to the downward carbon flux due to their high sinking rate (up to 50 m d^{-1}, Villa-Alfageme et al., 2016), and their ability to form large aggregates (Smetacek, 1985, 1999). Zooplankton also play a key role by repackaging organic matter into fecal pellets, thereby enhancing the speed at which it sinks out of the euphotic zone (Turner, 2002, 2015). Up to 90% of the exported material may be consumed and remineralized back into dissolved inorganic carbon (DIC) by heterotrophic activity in the mesopelagic zone (~100 - 1,000 m; Buesseler & Boyd, 2009; Kwon et al., 2009). Finally, a small fraction of this material may be sequestered in the bathypelagic zone (> 1,000 m) on timescales of months to millennia (Ducklow et al., 2001; Poulton et al., 2006).

In complement to the biological gravitational pump, Lévy et al. (2001), Omand et al. (2015) and Llort et al. (2018) provided evidence that export of organic matter also occurs through localized (1-10 km) eddy-driven subduction of non-sinking particles, and possibly dissolved organic carbon (DOC). In subpolar oceans, the eddy-driven subduction pump may contribute up to half of the total springtime export of POC (Omand et al., 2015). Through eddy-driven stratification, these submesoscale processes can also enhance the production of organic matter at the surface which will potentially be exported by subsequent eddy-driven subduction (Mahadevan et al., 2012; Omand et al., 2015). Submesoscale subduction thus leads to episodic injections of POC- and DOC-rich waters below the mixed layer, possibly outside the spring

bloom period. As current estimates of metabolic activity in the mesopelagic region exceed the influx of organic substrates generally attributed to the biological pump (Burd et al., 2010; Giering et al., 2014; Steinberg et al., 2008), submesoscale subduction has been invoked as an alternate pathway allowing a better balance of the carbon budget (Barth et al., 2002; Lévy et al., 2001; Omand et al., 2015). The spatial heterogeneity of this process could indeed stimulate hotspots of organic substrates, likely missed by conventional sampling methods.

Recently, Dall'Olmo et al. (2016) highlighted the global impact on carbon export budgets of seasonal detrainment of organic matter, a process known as the seasonal mixed layer pump (ML pump). A few localized studies had first described this mechanism at the diurnal timescale, showing that alternation of night convection and daily restratification can lead to an entrainment-detrainment cycle of particles from the mixed layer (Gardner et al., 1995; Ho & Marra, 1994; Woods & Onken, 1982). Indeed, the mixed layer deepens due to the effect of wind and heat loss to the atmosphere (Price et al., 1986) but does not shoal smoothly, as commonly assumed for the sake of simplicity. Instead, the upper-ocean stratifies due to solar heating or other sources (e.g. freshwater flux, slumping of isopycnals) and eventually a new mixed layer re-forms from the surface, thereby isolating phytoplankton cells and other particles in the so-called remnant layer (Franks, 2015; Ho & Marra, 1994; Fig. 1). At the diurnal timescale, the amplitude of the mixing layer depth variation is small (Woods & Onken, 1982) and much of the detrained organic material can be entrained back into the mixing layer. Thereby, the net export of carbon by the ML pump is accordingly weak. At the seasonal scale, however, the ML pump is a process of greater significance (Carlson et al., 1994; Dall'Olmo et al., 2016; Dall'Olmo & Mork, 2014). In springtime, the seasonal stratification of deep mixed layers contributes to export large amounts of carbon as dissolved organic matter or small non-sinking particles. In high-latitude regions with deep winter mixing, the seasonal ML pump amounts on average to 23% of the carbon supplied by fast sinking particles (Dall'Olmo et al., 2016).

The winter to spring evolution of the mixed layer depth (MLD) does not correspond to a smooth shoaling but rather is interspersed with restratification and deep mixing events (Lacour et al., 2017). Such intermittent mixing can enhance both phytoplankton production and POC export through the so-called intra-seasonal ML pump (Bishop et al., 1986; Garside & Garside, 1993; Giering et al., 2016; Koeve et al., 2002). When detrainment fluxes exceed entrainment fluxes, the intra-seasonal ML pump can lead to a net export of carbon to the mesopelagic. In the north-east Iceland basin, Giering et al. (2016) have shown that the pre-bloom flux of small particles driven by the ML pump can be of similar magnitude to the total particle export rate by sedimentation observed during, and after, the spring bloom period. However, the analysis of

long-term sediment trap data from 3000 m at the Porcupine Abyssal Plain (49°N, 16°W) revealed that pre-bloom deep fluxes are small (Lampitt et al., 2010). This discrepancy suggests that most of the particulate material exported by the ML pump is consumed in the mesopelagic zone (Giering et al., 2016), and potentially ventilated back into the atmosphere the following winter as inorganic carbon. Thus, this process may be less relevant to the long-term sequestration of carbon than for supplying energy to the mesopelagic food-web. In particular, zooplankton populations, especially overwintering organisms, inhabiting cold, dark and low turbulence environments at depth (Jónasdóttir et al., 2015; Steinberg & Landry, 2017; Visser et al., 2001) could benefit from the ML pump.

These three main pathways of carbon (i.e. the gravitational pump, the eddy-driven pump and the mixed layer pump) all contribute to the biological carbon pump (Dall'Olmo et al., 2016; Siegel et al., 2016; Llort et al., 2018). Indeed, they transfer organic matter from the productive mixing layer to the ocean interior where light and mixing are reduced. The amount of exported material determines the strength of the biological pump while the sequestration timescale control its efficiency (Buesseler & Boyd, 2009). For the particular case of the intra-seasonal ML pump, the strength is defined as the net amount of particulate organic carbon resulting from an entrainment-detrainment cycle.

Despite the recent discoveries mentioned above, the intra-seasonal dynamics of the ML pump and its potential role in sustaining mesopelagic ecosystems still remains poorly understood. The reason is twofold. First, current methods to estimate the depth of the mixed layer are not appropriate. Brainerd et al. (1995) highlighted the importance in distinguishing the mixed layer, the zone of relatively homogenous water formed by the history of mixing, from the mixing layer, the zone in which mixing is currently active. They showed that current density-derived methods fail to capture the high-frequency variability of the mixing layer. Second, most existing observational tools are not well suited to study such unpredictable episodic and widespread events. Using high-frequency sampling from autonomous profiling floats equipped with bio-optical sensors, we investigate here the intra-seasonal dynamics of the ML pump in the subpolar North Atlantic Ocean, a region that exhibits a strong spatiotemporal variability of the MLD. More specifically, we attempt to quantify the strength of the intra-seasonal ML pump on a basin scale, and characterize the nature and the fate of the exported material in the mesopelagic. The efficiency of this process in terms of long-term sequestration of carbon is not addressed. Rather, we discuss its importance in supplying pulses of fresh organic substrate to the mesopelagic ecosystem.

2 Material and Methods

2.1 The BGC-Argo dataset: description and data processing

The data used in this study were acquired by a fleet of 14 BGC-Argo floats that were deployed in the subpolar North Atlantic Ocean. These floats provided 2126 profiles spanning all seasons between 2014 and 2016 (Fig. 2). These floats (NKE PROVOR CTS-4) were equipped with: an SBE 41 CTD; a WET Labs ECO3 (Combined Three Channel Sensors) composed of a chlorophyll *a* (Chla) fluorometer, a Colored Dissolved Organic Matter (CDOM) fluorometer, and an optical backscattering sensor at 700 nm (b_{bp}); and an OCR-504 radiometer measuring Photosynthetically Available Radiation integrated over 400-700 nm (PAR). Measurements were collected during ascent every 2, 5 or 10 days, from 1,000 m (parking depth) to the surface. Vertical resolution of acquisition was 10 m between 1,000 m and 250 m, 1 m between 250 m and 10 m, and 0.2 m between 10 m and the surface. Radiometric measurements were acquired only in the upper 250 m. Data were transmitted through Iridium communication each time the floats surfaced, usually around local noon.

A "real time" quality control procedure was performed on the CTD data (Wong et al., 2015), Chla (Schmechtig et al., 2014) and PAR measurements (Organelli et al., 2016) after the factory calibrations were applied. The instrumental dark signal was removed from the Chla profile following the method in Xing et al. (2011) and the non-photochemical quenching (NPQ) was corrected as follows: the maximum Chla value above MLD, defined as a density difference of 0.01 kg m^{-3} with a reference value at 5 m, is extrapolated toward the surface. As an additional condition, the depth of the extrapolated Chla value has to be shallower than the depth of the isolume 20 µmol photons m^{-2} s^{-1} (derived from smoothed PAR profile), which marks approximatively the lower limit of the potential NPQ effect for mixed waters in this area (Lacour et al., 2017; Xing et al., 2018). Chla values were divided by a factor of 2 to account for a calibration systematic error in Wet Labs fluorometers (Roesler et al., 2017). Spikes were removed from Chla and b_{bp} profiles using a 5-point running median filter and a 7-point running mean filter similar to Briggs et al. (2011). The spike signals from b_{bp} profiles were used to detect large particles or aggregates following Briggs et al. (2011). Note that, because of the lower vertical resolution sampling below 250 m, deep spikes are not well resolved which potentially leads to an underestimation of large particles and aggregates. For the same reason, the depth correction for carbon loss relative to b_{bp} in aggregates used by Briggs et al. (2011) was not applied. Both baseline and spike signals from b_{bp} profiles were converted into POC using an empirical factor of 37,537 mg POC m^{-2} in the mixing layer and 31,519 mg POC m^{-2} below (Cetinić et al., 2012). This relationship might be biased by a background b_{bp} signal that

is not necessarily related to POC. Consequently, before converting to POC, the median of deep (950-1,000 m) b_{bp} values measured by each float was subtracted from each profile of the corresponding time series. POC derived from the baseline b_{bp} signal likely corresponds to small particles (0.2-20 µm; Dall'Olmo & Mork, 2014) whereas POC derived from spike signal corresponds to large particles or aggregates (Briggs et al., 2011). When not used as POC proxies, b_{bp} profiles are presented without the correction described above (i.e. removing deep values).

2.2 Atmospheric data

Net heat flux data were extracted from the ECMWF ERA Interim data set (reanalysis), freely available at http://apps.ecmwf.int/datasets/data/interim-full-daily/levtype=sfc. These data were averaged over 24-hour periods, with spatial resolution of 0.25°.

Wind stress data were extracted from the Ifremer CERSAT Global Blended Mean Wind Fields data set, freely available at http://marine.copernicus.eu/. This data set was estimated from scatterometers ASCAT and OSCAT retrievals and from ECMWF operational wind analysis with a horizontal resolution of 0.25° and 6 hours in time. Wind stress data were subsequently averaged over 24-hour periods to match net heat flux data. Wind stress τ was used to calculate the Ekman vertical length scale as follows: $Z_{Ek} = \gamma \frac{w_*}{f}$, where γ is an empirical constant of 0.5 (Wang & Huang, 2004), $f = 2 \times 7.29 \times 10^{-5} \times sin(latitude)$ is the Coriolis parameter and w_* is the turbulent friction velocity $w_* = \sqrt{\frac{\tau}{\rho_w}}$ with ρ_w the density of the surface water.

2.3 Estimation of mixing and mixed layer depths

A single criterion, the maximum vertical gradient, was used to estimate the mixing and mixed layer depths from Chla (maximum negative gradient) and density profiles (maximum positive gradient), respectively. To suppress the influence of spikes or noise, these profiles were additionally smoothed (Butterworth filter) before calculating the maximum gradient and the NPQ correction, which may erase a potential gradient, was performed after calculating the maximum gradient.

The maximum density gradient (MLD_{dens}) is interpreted to match the depth of the seasonal pycnocline (i.e. mixed layer depth), which is the envelope of the maximum depth reached by the mixing layer (Brainerd & Gregg, 1995). In contrast, the maximum Chla gradient (MLD_{bio}) should mark the mixing layer depth with time scales typical of phytoplankton growth (Boss & Behrenfeld, 2010; Zawada et al., 2005) (Fig. 1). The underlying concept is that Chla is

homogeneous over the whole mixing layer, if turbulent mixing overcomes vertical variations in the phytoplankton net growth rate (Huisman et al., 1999; Taylor & Ferrari, 2011). Indeed, while phytoplankton cells grow within the euphotic layer, mixing redistributes them throughout the mixing layer. However, as soon as cells are detrained from the mixing layer, the Chla signal starts to decrease in the remnant layer (Murphy & Cowles, 1997), hence intensifying the Chla gradient between mixing and remnant layers (Fig. 1). Figure 3 illustrates how MLD_{bio} can change within 2 days in response to change in atmospheric forcing, while MLD_{dens} remains deep as a signature of the past mixing event (on March 28th). As doubling time of phytoplankton cells is on the order of a day or more (Eppley et al., 1973; Goldman et al., 1979) MLD_{bio} is not likely able to capture the diurnal variability of the mixing layer. Thus, the typical timescale of the MLD_{bio} dynamics is 1-2 days. Considering the difference in timescale between MLD_{bio} and MLD_{dens}, we do not expect to have MLD_{bio} deeper than MLD_{dens} except in summer stratified conditions where phytoplankton can grow a few tens of meters below MLD_{dens}, depending on light penetration (see supplementary Fig. S1). Thus, MLD_{bio} estimation > 100 m deeper than MLD_{dens} is considered as an outlier. These outliers represent only 141 profiles, or 7% of the total data set.

2.4 Detection of submesoscale subduction events

Subduction is a 3-dimensional (3D) process involving lateral advection of water masses. Such a lateral advection can be identified on a 1D profile using a state variable called spice, based on anomalous temperature-salinity properties (Flament, 2002; McDougall & Krzysik, 2015; Omand et al., 2015). This variable is a useful indicator of interleaving of water masses. The relative standard deviation of a spice profile (RSDspice, standard deviation / mean) from surface (5 m) to MLD_{dens} is used to detect a potential intrusion of water in this layer. Application of this method over the entire dataset enables to roughly identify the submesoscale subduction events at a basin scale (Llort et al., 2018).

3 Results

3.1 Mixing versus Mixed layer dynamics

As proxies of the mixing and mixed layer depths, MLD_{bio} and MLD_{dens}, show different seasonal dynamics (Fig. 4). MLD_{bio} and MLD_{dens} are similar in fall and early winter, when strong atmospheric forcing induces turbulent mixing down to a depth that will define the upper limit of the seasonal pycnocline. During these periods, temperature, salinity and phytoplankton biomass are homogeneous down to MLD_{dens}. In late winter, MLD_{bio} and MLD_{dens} start to

diverge. Shallower mixing layers form above remnant layers, delimited by MLD_{bio} at the top and by MLD_{dens} at the bottom (Fig. 1). Phytoplankton in these remnant layers thus become isolated from the surface layer. In summer, MLD_{bio} is generally deeper than MLD_{dens} and likely corresponds to the lower limit of the euphotic zone. Light penetrates deeper than MLD_{dens} and allows phytoplankton growth below this layer (Fig. S1). Hence, regardless of the season, MLD_{bio} is a good indicator of the depth of the productive layer.

3.2 Impact of the mixing layer dynamics on POC export

The time series of a specific float (WMO 6901516, see the float trajectory in Fig. 2) is used to illustrate the impact of the mixing layer dynamics on POC export (Fig. 5). While MLD_{dens} roughly varies at the seasonal time scale, MLD_{bio} varies at higher frequency (Fig. 5b). MLD_{bio} oscillates between MLD_{dens} during convective mixing events (negative net heat flux, see Fig. 5c) and a shallower depth during stratification (positive heat flux) or shallow mixing events (i.e. wind-driven mixing, see Z_{Ek} on Fig. 5b).

High variability of the mixing layer occurs when net heat flux (Q) oscillates around zero during the winter-spring transition (March-May, Fig. 5c). The switch from negative to positive net heat flux is not a rapid smooth transition. Rather, it occurs over more than a one-month period and is associated with an intermittent reversal of the sign of this flux. This intermittency drives the high variability of MLD_{bio} which acts as a physical pump. Interestingly, zero-crossing net heat flux, in fall, does not affect the dynamics of MLD_{bio} which remains closely related to MLD_{dens}.

The water mass history of mixing can be retraced using a single 1D profile. Indeed, MLD_{bio} marks the depth limit of recently active mixing, while MLD_{dens} marks the depth limit of past mixing. Thus, the presence of a remnant layer can be identified and used as a signature of the ML pump. However, submesoscale subduction, which involves 3D processes, may also lead to similar signatures (Fig. S2). Therefore, profiles with RSD_{spice} higher than 5% were removed from the analysis in order to focus exclusively on ML pump-driven mechanisms. For the remaining profiles with a ML pump signature, it is assumed that each POC stock isolated in the remnant layer has been exported by the ML pump. In the present study, export is defined as the transfer of carbon from the turbulent productive layer to the low-turbulence remnant layer. In the area sampled by float 6901516, the POC stock transferred by the ML pump is maximal during the winter-spring transition when net heat fluxes switch from negative to positive values (up to 1.1 g C m^{-2}, see Fig. 5d). This maximum occurs before the main spring bloom (Fig. 5d and 5a). Occasionally, the contribution of large particles or aggregates to the POC stock can be significant (up to 88% during the winter-spring transition, see Fig. 5d).

On the basin scale, the temporal distribution of POC stocks transferred to the remnant layer presents a similar pattern. POC stocks significantly increase when the sign of the smoothed heat flux changes from negative to positive, with maximum values occurring 15 to 30 days later (Fig. 6a), and appear to be widespread over the whole subpolar region (Fig. 6b). Note that changing the RSD_{spice} threshold from 2.5 to 10% does not impact the distribution of POC stocks exported by ML pump events (see Fig. S3).

3.3 A quasi-Lagrangian approach to the ML pump

BGC-Argo floats are not Lagrangian floats and thus do not necessarily track coherent water masses. However, depending on the temporal resolution of the floats, some successive profiles may sample the same water mass, as evidenced by only subtle changes in hydrographic properties. Here, within 3 pre-defined layers (surface, remnant and deep layer), we used temperature, salinity and density differences of 0.1°C, 0.02 psu and 0.01 kg m^{-3} among consecutive profiles as criteria to identify sections of float trajectories with quasi-Lagrangian behaviors. We found only two sections that complied with these highly selective criteria (top panels in Fig. 7a and b). The first section contains 3 profiles from float 6901516 (yellow dots in Fig. 2) with 2-day intervals, and the second one contains 4 profiles from float 6901480 (green dots in Fig. 2) also with 2-day intervals. The first profile of each section is well mixed up to 250 m depth and 600 m depth for float 6901516 and 6901480 respectively. Then, mixing stops and a new mixing layer forms to a depth of around 100 m in both sections. The quasi-Lagrangian framework allows us to investigate the fate of Chla and b_{bp} within these 3 pre-defined layers (Fig. 7).

In new mixing layers (i.e. surface layers), both Chla and b_{bp} increase as a response to phytoplankton growth (triangles in Fig. 7). However, the accumulation rate of Chla ($\frac{1}{Chla}\frac{dChla}{dt}$ =0.15 d^{-1} and 0.16 d^{-1}) is higher than the accumulation rate of b_{bp} ($\frac{1}{b_{bp}}\frac{db_{bp}}{dt}$ =0.04 d^{-1} and 0.05 d^{-1}) for the full section period (4 days and 6 days) of float 6901516 and 6901480 respectively. In remnant layers, located in the twilight zone, both Chla and b_{bp} decrease, probably as a response to a change in the balance between production and heterotrophic consumption (circles in Fig. 7). Like surface layers, loss rate (i.e. negative accumulation rate) of Chla (0.1 d^{-1} and 0.06 d^{-1}) is higher than loss rate of b_{bp} (0.03 d^{-1} and 0.005 d^{-1}) for float 6901516 and 6901480 respectively. In deep layers, Chla and b_{bp} are stable with values near zero for Chla and values higher than $1x10^{-4}$ m^{-1} for b_{bp} (squares in Fig. 7). This deep b_{bp} signal is considered to be a constant background value.

As soon as the remnant layer forms and traps particles at depth, the Chla to b_{bp} ratio in this layer starts to decrease (Fig. 8). Thus, the Chla to b_{bp} ratio in the remnant layer can be considered as a relative proxy for the freshness of the exported material. A power law function, similar to the one used to calculate particle degradation in the ocean interior (Martin et al., 1987), has been fitted to the data to estimate an attenuation rate. Interestingly, in the remnant layer, the attenuation rate of the Chla to b_{bp} ratio over time is similar for both floats located in different regions of the subpolar North Atlantic (similar exponent in equations of Fig. 8a). Time series of Chla to b_{bp} ratio at each depth along the float trajectories 6901516 (February-July 2014) show that the ML pump export fresh material to depths ranging 0-340 m (mean 90 m) below MLD_{bio} during the whole winter-spring transition period (Fig. 9). Hence, the intermittent behavior of the ML pump in the winter-spring transition generates pulses of fresh organic material into the mesopelagic zone.

3.4 ML pump-driven POC flux estimates

We present here a method to estimate intra-seasonal ML pump-driven POC fluxes. The approach consists of calculating POC fluxes over a fixed time period on a basin scale (i.e. spatiotemporal binning), based on independent float profiles, i.e. without any assumption regarding float Lagrangian behavior.

A single ML pump event is defined by three successive steps: shallow mixing at time t_0 (i.e. initial conditions), deep mixing at time t_1 that leads to the entrainment of deep POC and restratification that leads to the detrainment of POC and the formation of the remnant layer observed at time t_2 (Fig. S4). The net POC flux is defined as the difference between the detrainment and entrainment fluxes, calculated as:

$$< E_{entrainment} > = \frac{< \int_{z=MLD_{bio_{t_0}}}^{z=MLD_{dens_{t_2}}} POC_{t_0}(z)\, dz >}{2 < \Delta t >} \quad (1)$$

$$< E_{detrainment} > = \frac{< POC_{t_1}(MLD_{dens\ t_2} - MLD_{bio\ t_2}) >}{2 < \Delta t >} \quad (2)$$

$$< E_{net} > = < E_{detrainment} > - < E_{entrainment} > \quad (3)$$

The numerator of equation 1 stands for the POC entrained by the deep mixing event at time t_1 while the numerator of equation 2 stands for the POC detrained during the restratification event

(Fig. S5). $MLD_{dens\ t_2}$ marks the depth limit of the deep mixing event and ($MLD_{dens\ t_2} - MLD_{bio\ t_2}$) represents the thickness of the remnant layer observed at time t_2. POC_{t_1}, the POC concentration within the deep mixing layer at time t_1, is estimated as the mean POC_{t_0} from the surface to $MLD_{dens\ t_2}$ (Fig. S5). Brackets indicate spatiotemporal binning. Δt is the time elapsed between the observation at time t_2 and the last mixing event at time t_1, and can be derived from the best-fit power law function in Fig. 8b as:

$$\Delta t = t_2 - t_1 = \left(\frac{Chla/b_{bp\ t_2} - Chla/b_{bp\ t_1}}{-0.11\ Chla/b_{bp\ t_1}}\right)^{\frac{1}{0.55}} \quad (4)$$

where $Chla/b_{bp\ t_2}$ is the ratio of the median Chla to the median b_{bp} within the remnant layer and $Chla/b_{bp\ t_1}$ is the ratio within the deep mixing layer at time t_1. $Chla/b_{bp\ t_1}$ is estimated the same way as POC_{t_1}, by averaging $Chla_{t_0}$ and $b_{bp\ t_0}$ from the surface to $MLD_{dens\ t_2}$. While $Chla/b_{bp\ t_2}$, $MLD_{dens\ t_2}$, and $MLD_{bio\ t_2}$ are measured at time t_2 when a remnant layer is identified (i.e. ML pump signature), initial conditions prevailing at time t_0 (i.e. $MLD_{bio_{t_0}}$, POC_{t_0}, $Chla_{t_0}$, $b_{bp\ t_0}$), from which variable at time t_1 are derived, are unknown. In order to provide a set of potential initial conditions for each profile with a ML pump signature, all available profiles, from 2014 to 2016, within a radius of 300 km and a time period of 15 days (all years included), are collected (Fig. S6). To keep only realistic initial conditions, three requisites are needed: 1) $Chla/b_{bp\ t_1}$, derived from $Chla_{t_0}$ and $b_{bp\ t_0}$, is higher than $Chla/b_{bp\ t}$, 2) $MLD_{bio_{t_0}}$ is shallower than $MLD_{dens\ t_2}$, 3) Δt is less than 20 days. The choice of a threshold of 20 days is based on the basin-scale analysis of the density function of $Chla/b_{bp}$ both within the mixing and remnant layers (Fig. S7). Using the attenuation rate of $Chla/b_{bp}$ shown in Fig. 8b, we modeled the cumulative density function within the remnant layer for Δt ranging from 1 to 5, 20 or 35 days (see caption of Fig. S7) and compared it with the measured cumulative density function. The cumulative density function for Δt ranging from 1 to 20 days is the one which best fit the measured density function within the remnant layer. Therefore, a threshold of 20 days seems appropriate to reject unrealistic initial conditions. All the initial conditions that complied with these 3 requisites are used to calculate a mean Δt and associated standard deviation for each profile presenting a ML pump signature. Over a fixed time period, the mean duration of ML pump events is estimated as $2 < \Delta t >$ (Fig. S8). Indeed, as the profiling time t_2 is random between the last mixing event at time t_1 and the next one,

potentially at t_3, Δt should range from 0 to $(t_3 - t_1)$, with mean value $< \Delta t > = (t_3 - t_1)/2$. Here, a time period of 10 days is used, with a minimum of 6 profiles as an additional requirement to correctly estimate the mean duration of ML pump events.

Figure 10 presents estimates of entrainment, detrainment and net POC fluxes averaged over 10-day periods in the whole subpolar North Atlantic Ocean. As expected, the temporal pattern in detrainment fluxes (Fig. 10c) is similar to the one observed in POC stock in the remnant layer (Fig. 6a) and the one in detrained POC stocks estimated from initial conditions (Fig. 10a, numerators in equation 2, blue color). Maximum detrainment fluxes and net export fluxes (125 and 55 mg C m^{-2} d^{-1}, respectively) both occur few days after the switch in the sign of the heat flux. Approximately 40 days later, detrainment fluxes decrease by a factor of 2 to 3 and net POC fluxes are reduced to near zero. The length of error bars represents the average standard deviation of initial conditions associated to each ML pump signature detected within a 10-day time period. Note that fluxes were not estimated between days 70 to 90 because the number of profiles presenting a ML pump signature was below the critical threshold of 6 profiles (Fig. S8).

4 Discussion

4.1 Mixing versus mixed layer depth

Observations of vertical profiles of density and Chla in late winter and spring (Fig. 4) suggest that density-derived methods to estimate MLD have to be interpreted with caution when considering controls on phytoplankton processes. A simple comparison (linear correlation analysis, Fig. S9) between MLD_{bio} and MLD estimated with different density-difference criteria revealed that most of these criteria do not detect subtle changes in density, which affect the phytoplankton vertical distribution (Lacour et al., 2017). As a consequence, studies estimating depth-integrated Chla by multiplying the concentration of surface Chla (measured by satellite) by the depth of a density-derived mixed layer could overestimate the Chla stock, especially during the winter to spring transition. Indeed, the widely used density difference criteria of 0.1 kg m^{-3} leads, in the present study, to a mean overestimation of 46% of the spring phytoplankton stock (comparison of the real stock measured by the float in the mixed layer with the estimated stock based on surface Chla). However, a density criterion of 0.01 kg m^{-3}, which shows the best correlation with MLD_{bio}, leads to a mean overestimation of only 3%. Most density difference thresholds are not suited to capture the intra-seasonal dynamics of the mixing layer which affects the vertical distribution of phytoplankton biomass.

4.2 The ML pump signature

The ML pump is a complex mechanism which can occur on a variety of timescales, from diurnal to seasonal scales. Observing this mechanism at specific scales requires appropriate approaches. Combining Argo float data with satellite estimates of POC, Dall'Olmo et al. (2016) provided first estimates of the carbon flux induced by the seasonal ML pump at global scale. The rate of change of the MLD at a time interval of 10 days along Argo float trajectories was exploited. Therefore, the high-frequency variability (< 10 days) was not considered and assumption of spatial homogeneity was required. This approach revealed the importance of the ML pump in seasonal carbon fluxes but the episodic nature of carbon export was not considered. The innovative approach, here, is to use a single profile to retrace the water mass history of mixing and thus relax the assumption of spatial homogeneity. Using MLD_{bio} as the depth limit of a recent mixing and MLD_{dens} as the depth limit of a past mixing, the presence of a remnant layer can be identified and used as a signature of the ML pump. Although the typical timescale of MLD_{bio} is known (~1-2 days), the timescale of MLD_{dens} is more difficult to assess. Figure 3b shows that MLD_{dens} is still deep 4 days after deep convection stopped and figure 5b reveals a ~10-day delay between the permanent shoaling of MLD_{bio} around 100 m and the shoaling of MLD_{dens}. It is thus assumed that MLD_{dens} roughly corresponds to a mixed layer on a 10-day timescale. Thereby, the signature of ML pump likely reveals recent export of organic matter thus allowing the assessment of the episodic nature of this mechanism. Although this approach allows exploration of the intra-seasonal dynamics of the ML pump, the diurnal timescales are not assessed.

The strongest signatures of the ML pump (i.e. maximum POC stock in the remnant layer) were recorded when the net heat flux switches from negative to positive values in early spring. Interestingly, the switch from positive to negative values in fall did not affect MLD_{bio} which remained closely related to MLD_{dens} (Fig. 5). This dissymmetry was likely due to the mechanical effect of wind, that mixes the upper layer (Woods, 1980). The Ekman length scale, which is the dominant mixing length scale when heat fluxes are small (Brody & Lozier, 2014), indicated that mixing reached depths as deep as MLD_{dens} at this time of the year (Fig. 5b). Phytoplankton can be redistributed within MLD_{dens} even if net heat fluxes become positive, thus inhibiting the formation of remnant layers.

Warming of the upper layer is not the only source of stratification. In addition to freshwater flux, 3D processes involving lateral advection are known to quickly restratify deep mixed layers (Brainerd & Gregg, 1993; Hosegood et al., 2006, 2008; Johnson et al., 2016). Submesoscale eddies or Ekman buoyancy flux can slump horizontal density gradient to create vertical

stratification (Boccaletti et al., 2007; Thomas & Lee, 2005). These processes, which generate a signature similar to the ML pump, are often associated with submesoscale subduction (Omand et al., 2015). Based on a RSD_{spice} threshold of 5%, it can be estimated that almost 40% of the profiles displaying a ML pump signature were affected by lateral water intrusion. As mentioned by Ho and Marra (1994), quantifying ML pump export is difficult since local and advective effects have to be distinguished. Here, a RSD_{spice} threshold of 5% appeared adequate to identify and subsequently remove profiles affected by advective effects. However, it is worth noting that lateral restratifications could contribute to the export through the ML pump. Indeed, lateral restratification can stimulate phytoplankton production (Mahadevan et al., 2012), even during winter (Lacour et al., 2017), and the resulting biomass could be exported later, following a deep mixing event. Although this study focuses on 1D processes, lateral restratification may also stimulate the ML pump export, especially in winter when positive heat flux events are scarcer.

4.3 Fate of Chla and b_{bp} signal in the remnant layer

Quasi-Lagrangian sections of float trajectories allowed us to investigate the fate of Chla and b_{bp} signals in surface and remnant layers after a stratification event (Fig. 7). Chla signals increased faster in the surface layer and decreased faster in the remnant layer than the b_{bp} signals. The main reason for this discrepancy rests on the nature of the particles contributing to both Chla and b_{bp} signal. While phytoplankton cells contribute nearly all of the Chla signal (colored dissolve organic matter may also contribute slightly to the Chla signal; Xing et al., 2017), bacteria, protists, detritus and mineral material also contribute to the b_{bp} signal (Martinez-Vicente et al., 2012; Stramski et al., 1991, 2001, 2004). Therefore, in the surface layer, an increase in phytoplankton production does not lead to a similar relative increase in the Chla and b_{bp} signals. In addition, taxonomic changes in the phytoplankton community could further increase the Chla signal relative to the b_{bp} signal. Indeed, the local restratification could enhance the light environment and stimulate larger phytoplankton, such as diatoms, with higher Chla to b_{bp} ratio (Cetinić et al., 2015; Lacour et al., 2017; Rembauville et al., 2017). In the twilight remnant layer, change in the balance between production and consumption leads to a decrease in both Chla and b_{bp}. However, the faster decrease in the Chla signal may be explained by multiple factors. First, fresh phytoplankton (i.e. Chla signal) are possibly preferentially consumed compared to detritus and other material contributing to the b_{bp} signal. Second, the consumption of phytoplankton cells could enhance the growth of heterotrophic organisms such as bacteria or protists which would also contribute to the b_{bp} signal. Third, physical and biological disaggregation of large particles at depth (Alldredge et al., 1990; Burd & Jackson,

2009; Cho & Azam, 1988) may enhance the b_{bp} signal, which likely corresponds to small particles (0.2-20 µm; Dall'Olmo & Mork, 2014), and counteract the decrease in b_{bp} due to consumption. Finally, additional decrease in Chla could be attributed to physiological adaptations to darkness which involve a reduced fluorescence per unit of Chla (Murphy & Cowles, 1997).

4.4 Towards global event-based POC flux estimates

Present carbon flux estimates are mainly based on a limited number of observations at specific times and locations. Scaling up these observations to obtain regional and global estimates may neglect or underestimate the contribution of episodic events, leading to our inability to balance biogeochemical budgets in the mesopelagic (Burd et al., 2016). The ML pump is a typical mechanism driving episodic export of organic carbon to depth. Based on high-resolution observations from a dense BGC-Argo float network, we assessed for the first time the intra-seasonal dynamics of ML pump-driven POC fluxes on a basin scale (Fig. 10). This approach required three main assumptions:

(1) We assumed that initial conditions (i.e. $\mathrm{Chla}/\mathrm{b_{bp}}_{t_0}$, $\mathrm{POC}_{\mathrm{MLD_{bio}}\,t_0}$) prevailing before a ML pump event can be predicted from a "climatology" of profiles collected in the area of the event location. Three selection criteria (see section 3.4) have been applied to ensure that only realistic initial conditions have been used. Error bars in figure 10a and b show that the variability related to these initial conditions remains reasonably small.

(2) We assumed that the mean duration of ML pump events is twice the mean time $< \Delta t >$ between the observation of the ML pump signature and the last mixing event. An analysis of ML pump events recorded by a Lagrangian float revealed that the absolute error related to this assumption is less than 0.2 days as long as the number of events averaged is more than 6 (Fig. S6). As the BGC-Argo dataset will expand in the future, we will be able to reduce the spatiotemporal binning with the goal of quantifying event-based POC fluxes on a basin scale.

(3) The attenuation rate of the Chla to b_{bp} ratio in the remnant layer is assumed to be constant on a basin scale. The present analysis demonstrated that this attenuation rate is similar within two different regions of the subpolar North Atlantic. However, additional measurements in remnant layers are clearly needed to better constrain the attenuation rate of the Chla to b_{bp} ratio and reduce uncertainties associated to this approach. More generally, further investigations on particle composition, microbial metabolism and

transformation processes occurring in remnant layers are required to better understand the fate of the organic material exported by the ML pump.

The mean ML pump-driven net POC flux peaks at 55 mg C m^{-2} d^{-1} in late winter and drops down to negative values when the water column stabilizes in summer. During this period, the entrainment flux due to wind-driven mixing events can exceed the detrainment flux, as the light penetration allows phytoplankton to grow below the mixing layer. The net amount of POC exported during the winter-spring transition (i.e. positive net export) is the fraction of fresh organic material that we expect to be consumed in the mesopelagic. Therefore, the intra-seasonal ML pump may sustain the mesopelagic ecosystem before the spring bloom period.

4.5 Role of the ML pump in sustaining mesopelagic ecosystems

The recurrence of widespread ML pump events during a relatively large time period (> 90 days) implies that this mechanism may be of great significance in supplying the energy required by the mesopelagic heterotrophic community (Dall'Olmo et al., 2016). The particles mixed downward through the ML pump are rich in fresh phytoplankton and detritus, so potentially of high nutritional content for grazers located below the mixing layer (Steinberg & Landry, 2017). Export of both small and large particles to the mesopelagic region suggests that this mechanism could sustain zooplankton populations with different feeding preferences (Fenchel, 1980; Irigoien et al., 2000; Turner et al., 2001; Turner, 2004). Products from zooplankton activities would then sustained microbial populations and higher trophic levels (Steinberg & Landry, 2017). Therefore, the ML pump could supply a major source of energy to the whole mesopelagic ecosystem during the winter to spring transition.

Many studies reported that the bulk of zooplankton populations resides just below the turbulent mixing layer (Incze et al., 2001; Lagadeuc et al., 1997; Mackas et al., 1993). The turbulence-avoidance behavior of grazers has been invoked to explain their vertical distribution in the water column (Franks, 2001). However, the reason for this behavior is not clear. Turbulence is known to influence encounter and ingestion rate of zooplankton and larger predators, but both positive and negative effects have been reported (MacKenzie, 2000). During the winter to spring transition, the vertical distribution of grazers could be a direct consequence of the ML pump. These organisms could swim deep during turbulent mixing events, then immediately return to the remnant layer upon restratification to take advantage of fresh food supplied by the ML pump. For this reason, export is defined here as a transfer from the turbulent productive layer to the remnant non-productive layer.

Finally, the ML pump during the winter-spring transition could trigger the seasonal development of overwintering organisms such as copepods so that their reproduction would coincide with the forthcoming spring bloom (Bishop & Wood, 2009). We can thus speculate that the frequency of episodic ML pump export events during the pre-bloom period may modulate the timing of the maturation phase of copepods and indirectly impact the magnitude of the spring bloom.

5 Conclusion

The density of the BGC-Argo float network has enabled, for the first time, investigation of the intra-seasonal dynamics of the ML pump on a basin scale. ML pump signatures are widespread over the subpolar North Atlantic Ocean and span a large temporal window preceding the spring bloom. To date, the high-frequency dynamics of bio-physical mechanisms had clearly been overlooked due to the lack of well-suited observational tools. Yet, ML pump episodic events may contribute significantly to the export of fresh organic matter during the late winter and early spring periods. This mechanism may sustain the development of overwintering organisms such as copepods with potential impact on the characteristics of the forthcoming spring phytoplankton bloom through predator-prey interactions. Further investigations of episodic events will undoubtedly provide new insights on life strategies and food web interactions, and potentially address the fundamental limitations of assuming steady-state conditions.

Acknowledgments

This work represents a contribution to the REMOCEAN project (REMotely sensed biogeochemical cycles in the OCEAN, GA 246777) funded by the European Research Council and the ATLANTOS EU project (grant agreement 2014-633211) funded by H2020 program. BGC-Argo data are publicly available at ftp://ftp.ifremer.fr/ifremer/argo/dac/coriolis/. We thank C. Schmechtig and A. Poteau for BGC-Argo float data management and M. Gali for fruitful discussions.

References

Alldredge, A. L., Granata, T. C., Gotschalk, C. C., & Dickey, T. D. (1990). The physical strength of marine snow and its implications for particle disaggregation in the ocean. *Limnology and Oceanography*, *35*(7), 1415–1428. https://doi.org/10.4319/lo.1990.35.7.1415

Barth, J. A., Cowles, T. J., Kosro, P. M., Shearman, R. K., Huyer, A., & Smith, R. L. (2002). Injection of carbon from the shelf to offshore beneath the euphotic zone in the California Current. *Journal of Geophysical Research*, *107*(C6), 3057.

https://doi.org/10.1029/2001JC000956
Bishop, J. K. B., Conte, M. H., Wiebe, P. H., Roman, M. R., & Langdon, C. (1986). Particulate matter production and consumption in deep mixed layers: observations in a warm-core ring. *Deep Sea Research Part A. Oceanographic Research Papers*, *33*(11–12), 1813–1841. https://doi.org/10.1016/0198-0149(86)90081-6
Bishop, J. K. B., & Wood, T. J. (2009). Year-round observations of carbon biomass and flux variability in the Southern Ocean. *Global Biogeochemical Cycles*, *23*(2), n/a-n/a. https://doi.org/10.1029/2008GB003206
Boccaletti, G., Ferrari, R., & Fox-Kemper, B. (2007). Mixed Layer Instabilities and Restratification. *Journal of Physical Oceanography*, *37*(9), 2228–2250. https://doi.org/10.1175/JPO3101.1
Boss, E., & Behrenfeld, M. (2010). In situ evaluation of the initiation of the North Atlantic phytoplankton bloom. *Geophysical Research Letters*, *37*(18). https://doi.org/10.1029/2010GL044174
Brainerd, K. E., & Gregg, M. C. (1993). Diurnal restratification and turbulence in the oceanic surface mixed layer: 1. Observations. *Journal of Geophysical Research*, *98*(C12), 22645. https://doi.org/10.1029/93JC02297
Brainerd, K. E., & Gregg, M. C. (1995). Surface mixed and mixing layer depths. *Deep-Sea Research Part I*, *42*(9), 1521–1543. https://doi.org/10.1016/0967-0637(95)00068-H
Briggs, N., Perry, M. J., Cetinić, I., Lee, C., D'Asaro, E., Gray, A. M., & Rehm, E. (2011). High-resolution observations of aggregate flux during a sub-polar North Atlantic spring bloom. *Deep Sea Research Part I: Oceanographic Research Papers*, *58*(10), 1031–1039. https://doi.org/10.1016/j.dsr.2011.07.007
Brody, S. R., & Lozier, M. S. (2014). Changes in dominant mixing length scales as a driver of subpolar phytoplankton bloom initiation in the North Atlantic. *Geophysical Research Letters*, *41*(9), 3197–3203. https://doi.org/10.1002/2014GL059707
Buesseler, K. O., & Boyd, P. W. (2009). Shedding light on processes that control particle export and flux attenuation in the twilight zone of the open ocean. *Limnology and Oceanography*, *54*(4), 1210–1232. https://doi.org/10.4319/lo.2009.54.4.1210
Burd, A. B., Hansell, D. A., Steinberg, D. K., Anderson, T. R., Arístegui, J., Baltar, F., … Tanaka, T. (2010). Assessing the apparent imbalance between geochemical and biochemical indicators of meso- and bathypelagic biological activity: What the @$#! is wrong with present calculations of carbon budgets? *Deep-Sea Research Part II: Topical Studies in Oceanography*, *57*(16), 1557–1571. https://doi.org/10.1016/j.dsr2.2010.02.022
Burd, A. B., & Jackson, G. A. (2009). Particle Aggregation. *Annual Review of Marine Science*, *1*(1), 65–90. https://doi.org/10.1146/annurev.marine.010908.163904
Burd, A., Buchan, A., Church, M., Landry, M., McDonnell, A., Passow, U., … Benway, H. (2016). *Towards a transformative understanding of the ocean ' s biological pump : Priorities for future research*. *Report of the NSF Biology of the Biological Pump Workshop, February 19-20, 2016*. Woods Hole, MA: Ocean Carbon and Biogeochemistry (OCB) Program. https://doi.org/10.1575/1912/8263
Carlson, C. A., Ducklow, H. W., & Michaels, A. F. (1994). Annual flux of dissolved organic carbon from the euphotic zone in the northwestern Sargasso Sea. *Nature*, *371*(6496), 405–408. https://doi.org/10.1038/371405a0
Cetinić, I., Perry, M. J., Briggs, N. T., Kallin, E., D'Asaro, E. a., & Lee, C. M. (2012). Particulate organic carbon and inherent optical properties during 2008 North Atlantic Bloom Experiment. *Journal of Geophysical Research*, *117*(C6), C06028. https://doi.org/10.1029/2011JC007771
Cetinić, I., Perry, M. J., D'Asaro, E., Briggs, N., Poulton, N., Sieracki, M. E., & Lee, C. M. (2015). A simple optical index shows spatial and temporal heterogeneity in

610 phytoplankton community composition during the 2008 North Atlantic Bloom
611 Experiment. *Biogeosciences*, *12*(7), 2179–2194. https://doi.org/10.5194/bg-12-2179-
612 2015
613 Cho, B. C., & Azam, F. (1988). Major role of bacteria in biogeochemical fluxes in the ocean's
614 interior. *Nature*. https://doi.org/10.1038/332441a0
615 Dall'Olmo, G., Dingle, J., Polimene, L., Brewin, R. J. W., & Claustre, H. (2016). Substantial
616 energy input to the mesopelagic ecosystem from the seasonal mixed-layer pump. *Nature*
617 *Geoscience*. https://doi.org/10.1038/ngeo2818
618 Dall'Olmo, G., & Mork, K. A. (2014). Carbon export by small particles in the Norwegian
619 Sea. *Geophysical Research Letters*, *41*(8), 2921–2927.
620 https://doi.org/10.1002/2014GL059244
621 Ducklow, H., Steinberg, D., & Buesseler, K. (2001). Upper Ocean Carbon Export and the
622 Biological Pump. *Oceanography*, *14*(4), 50–58. https://doi.org/10.5670/oceanog.2001.06
623 Eppley, R. W., Renger, E. H., Venrick, E. L., Mullin, M. M., & Jul, N. (1973). A Study of
624 Plankton Dynamics and Nutrient Cycling in the Central Gyre of the North Pacific Ocean.
625 *Limnology and Oceanography*, *18*(4), 534–551.
626 https://doi.org/10.4319/lo.1973.18.4.0534
627 Fenchel, T. (1980). Suspension feeding in ciliated protozoa: Functional response and particle
628 size selection. *Microbial Ecology*, *6*(1), 1–11. https://doi.org/10.1007/BF02020370
629 Franks, P. J. S. (2001). Turbulence avoidance: An alternate explanation of turbulence-
630 enhanced ingestion rates in the field. *Limnology and Oceanography*, *46*(4), 959–963.
631 https://doi.org/10.4319/lo.2001.46.4.0959
632 Gardner, W. D., Chung, S. P., Richardson, M. J., & Walsh, I. D. (1995). The oceanic mixed-
633 layer pump. *Deep Sea Research Part II: Topical Studies in Oceanography*, *42*(2–3),
634 757–775. https://doi.org/10.1016/0967-0645(95)00037-Q
635 Garside, C., & Garside, J. C. (1993). The "f-ratio" on 20°W during the North Atlantic Bloom
636 Experiment. *Deep-Sea Research Part II*, *40*(1–2), 75–90. https://doi.org/10.1016/0967-
637 0645(93)90007-A
638 Giering, S. L. C., Sanders, R., Lampitt, R. S., Anderson, T. R., Tamburini, C., Boutrif, M., …
639 Mayor, D. J. (2014). Reconciliation of the carbon budget in the ocean's twilight zone.
640 *Nature*, *507*(7493), 480–483. https://doi.org/10.1038/nature13123
641 Giering, S. L. C., Sanders, R., Martin, A. P., Lindemann, C., Möller, K. O., Daniels, C. J., …
642 St. John, M. A. (2016). High export via small particles before the onset of the North
643 Atlantic spring bloom. *Journal of Geophysical Research: Oceans*, *121*(9), 6929–6945.
644 https://doi.org/10.1002/2016JC012048
645 Goldman, J. C., McCarthy, J. J., & Peavey, D. G. (1979). Growth rate influence on the
646 chemical composition of phytoplankton in oceanic waters. *Nature*, *279*(5710), 210–215.
647 https://doi.org/10.1038/279210a0
648 Ho, C., & Marra, J. (1994). Early-spring export of phytoplankton production in the northeast
649 Atlantic Ocean. *Marine Ecology Progress Series*, *114*(1), 197–202.
650 https://doi.org/10.3354/meps114197
651 Hosegood, P., Gregg, M. C., & Alford, M. H. (2006). Sub-mesoscale lateral density structure
652 in the oceanic surface mixed layer. *Geophysical Research Letters*, *33*(22), L22604.
653 https://doi.org/10.1029/2006GL026797
654 Hosegood, P. J., Gregg, M. C., & Alford, M. H. (2008). Restratification of the Surface Mixed
655 Layer with Submesoscale Lateral Density Gradients: Diagnosing the Importance of the
656 Horizontal Dimension. *Journal of Physical Oceanography*, *38*(11), 2438–2460.
657 https://doi.org/10.1175/2008JPO3843.1
658 Huisman, J., Oostveen, P. van, & Weissing, F. J. (1999). Critical Depth and Critical
659 Turbulence: Two Different Mechanisms for the Development of Phytoplankton Blooms.

Limnology and Oceanography, *44*(7), 1781–1787. Retrieved from http://www.jstor.org/stable/2670414

Incze, L., Hebert, D., Wolff, N., Oakey, N., & Dye, D. (2001). Changes in copepod distributions associated with increased turbulence from wind stress. *Marine Ecology Progress Series*, *213*, 229–240. https://doi.org/10.3354/meps213229

Irigoien, X., Harris, R. P., Head, R. N., & Harbour, D. (2000). The influence of diatom abundance on the egg production rate of Calanus helgolandicus in the English Channel. *Limnology and Oceanography*, *45*(6), 1433–1439. https://doi.org/10.4319/lo.2000.45.6.1433

Johnson, L., Lee, C. M., & D'Asaro, E. A. (2016). Global Estimates of Lateral Springtime Restratification. *Journal of Physical Oceanography*, *46*(5), 1555–1573. https://doi.org/10.1175/JPO-D-15-0163.1

Jónasdóttir, S. H., Visser, A. W., Richardson, K., & Heath, M. R. (2015). Seasonal copepod lipid pump promotes carbon sequestration in the deep North Atlantic. *Proceedings of the National Academy of Sciences*, *112*(39), 12122–12126. https://doi.org/10.1073/pnas.1512110112

Koeve, W., Pollehne, F., Oschlies, A., & Zeitzschel, B. (2002). Storm-induced convective export of organic matter during spring in the northeast Atlantic Ocean. *Deep-Sea Research Part I: Oceanographic Research Papers*, *49*(8), 1431–1444. https://doi.org/10.1016/S0967-0637(02)00022-5

Kwon, E. Y., Primeau, F., & Sarmiento, J. L. (2009). The impact of remineralization depth on the air-sea carbon balance. *Nature Geoscience*, *2*(9), 630–635. https://doi.org/10.1038/ngeo612

Lacour, L., Ardyna, M., Stec, K. F., Claustre, H., Prieur, L., Poteau, A., … Iudicone, D. (2017). Unexpected winter phytoplankton blooms in the North Atlantic subpolar gyre. *Nature Geoscience*, *10*(11), 836–839. https://doi.org/10.1038/NGEO3035

Lagadeuc, Y., Boulé, M., & Dodson, J. J. (1997). Effect of vertical mixing on the vertical distribution of copepods in coastal waters. *Journal of Plankton Research*, *19*(9), 1183–1204. https://doi.org/10.1093/plankt/19.9.1183

Lampitt, R. S., Salter, I., de Cuevas, B. A., Hartman, S., Larkin, K. E., & Pebody, C. A. (2010). Long-term variability of downward particle flux in the deep northeast Atlantic: Causes and trends. *Deep-Sea Research Part II: Topical Studies in Oceanography*, *57*(15), 1346–1361. https://doi.org/10.1016/j.dsr2.2010.01.011

Lévy, M., Klein, P., & Treguier, A.-M. (2001). Impact of sub-mesoscale physics on production and subduction of phytoplankton in an oligotrophic regime. *Journal of Marine Research*, *59*(4), 535–565. https://doi.org/10.1357/002224001762842181

Llort, J., Langlais, C., Matear, R., Moreau, S., Lenton, A., & Strutton, P. G. (2018). Evaluating Southern Ocean Carbon Eddy-Pump From Biogeochemical-Argo Floats. *Journal of Geophysical Research: Oceans*, *123*(2), 971–984. https://doi.org/10.1002/2017JC012861

Mackas, D. L., Sefton, H., Miller, C. B., & Raich, A. (1993). Vertical habitat partitioning by large calanoid copepods in the oceanic subarctic Pacific during Spring. *Progress in Oceanography*, *32*(1), 259–294. https://doi.org/10.1016/0079-6611(93)90017-8

MacKenzie, B. R. (2000). Turbulence, larval fish ecology and fisheries recruitment: a review of field studies. *Oceanologica Acta*, *23*(4), 357–375. https://doi.org/10.1016/S0399-1784(00)00142-0

Mahadevan, a., D'Asaro, E., Lee, C., & Perry, M. J. (2012). Eddy-Driven Stratification Initiates North Atlantic Spring Phytoplankton Blooms. *Science*, *337*(6090), 54–58. https://doi.org/10.1126/science.1218740

Martin, J. H., Knauer, G. A., Karl, D. M., & Broenkow, W. W. (1987). VERTEX: carbon

cycling in the northeast Pacific. *Deep Sea Research Part A. Oceanographic Research Papers*, *34*(2), 267–285. https://doi.org/https://doi.org/10.1016/0198-0149(87)90086-0

Martin, P., Lampitt, R. S., Jane Perry, M., Sanders, R., Lee, C., & D'Asaro, E. (2011). Export and mesopelagic particle flux during a North Atlantic spring diatom bloom. *Deep Sea Research Part I: Oceanographic Research Papers*, *58*(4), 338–349. https://doi.org/10.1016/j.dsr.2011.01.006

Martinez-Vicente, V., Tilstone, G., Sathyendranath, S., Miller, P., & Groom, S. (2012). Contributions of phytoplankton and bacteria to the optical backscattering coefficient over the Mid-Atlantic Ridge. *Marine Ecology Progress Series*, *445*, 37–51. https://doi.org/10.3354/meps09388

Murphy, A. M., & Cowles, T. J. (1997). Effects of darkness on multi-excitation in vivo fluorescence and survival in a marine diatom. *Limnology and Oceanography*, *42*(6), 1444–1453. https://doi.org/10.4319/lo.1997.42.6.1444

Omand, M. M., D'Asaro, E. A., Lee, C. M., Perry, M. J., Briggs, N., Cetinić, I., & Mahadevan, A. (2015). Eddy-driven subduction exports particulate organic carbon from the spring bloom. *Science*, *348*(6231), 222–225. https://doi.org/10.1126/science.1260062

Organelli, E., Claustre, H., Bricaud, A., Schmechtig, C., Poteau, A., Xing, X., … Vellucci, V. (2016). A novel near-real-time quality-control procedure for radiometric profiles measured by bio-argo floats: Protocols and performances. *Journal of Atmospheric and Oceanic Technology*, *33*(5), 937–951. https://doi.org/10.1175/JTECH-D-15-0193.1

Poulton, A. J., Holligan, P. M., Hickman, A., Kim, Y.-N., Adey, T. R., Stinchcombe, M. C., … Woodward, E. M. S. (2006). Phytoplankton carbon fixation, chlorophyll-biomass and diagnostic pigments in the Atlantic Ocean. *Deep Sea Research Part II: Topical Studies in Oceanography*, *53*(14–16), 1593–1610. https://doi.org/10.1016/j.dsr2.2006.05.007

Price, J. F., Weller, R. A., & Pinkel, R. (1986). Diurnal Cyciling: Observation and models of the upper ocean response to diurnal heating, cooling and wind mixing. *Journal of Geophysical Research*, *91*, 8411–8427. https://doi.org/10.1029/JC091iC07p08411

Rembauville, M., Briggs, N., Ardyna, M., Uitz, J., Catala, P., Penkerc'ch, C., … Blain, S. (2017). Plankton Assemblage Estimated With BGC-Argo Floats in the Southern Ocean: Implications for Seasonal Successions and Particle Export. *Journal of Geophysical Research: Oceans*. https://doi.org/10.1002/2017JC013067

Roesler, C., Uitz, J., Claustre, H., Boss, E., Xing, X., Organelli, E., … Barbieux, M. (2017). Recommendations for obtaining unbiased chlorophyll estimates from in situ chlorophyll fluorometers: A global analysis of WET Labs ECO sensors. *Limnology and Oceanography: Methods*, *15*(6), 572–585. https://doi.org/10.1002/lom3.10185

Sanders, R., Henson, S. A., Koski, M., De La Rocha, C. L., Painter, S. C., Poulton, A. J., … Martin, A. P. (2014). The Biological Carbon Pump in the North Atlantic. *Progress in Oceanography*, *129*(PB), 200–218. https://doi.org/10.1016/j.pocean.2014.05.005

Schmechtig, C., Claustre, H., Poteau, A., & D'Ortenzio, F. (2014). Bio-Argo quality control manual for the Chlorophyll-A concentration. *Ifremer*, 13. https://doi.org/http://dx.doi.org/10.13155/35385 Bio-Argo

Siegel, D. A., Buesseler, K. O., Behrenfeld, M. J., Benitez-Nelson, C. R., Boss, E., Brzezinski, M. A., … Steinberg, D. K. (2016). Prediction of the Export and Fate of Global Ocean Net Primary Production: The EXPORTS Science Plan. *Frontiers in Marine Science*, *3*, 22. https://doi.org/10.3389/fmars.2016.00022

Smetacek, V. (1999). Diatoms and the ocean carbon cycle. *Protist News*, *150*(1), 25–32. https://doi.org/10.1016/S1434-4610(99)70006-4

Smetacek, V. S. (1985). Role of sinking in diatom life-history cycles: ecological, evolutionary and geological significance. *Marine Biology*, *84*(3), 239–251. https://doi.org/10.1007/BF00392493

760 Steinberg, D. K., & Landry, M. R. (2017). Zooplankton and the Ocean Carbon Cycle. *Annual*
761 *Review of Marine Science*, *9*(1). https://doi.org/10.1146/annurev-marine-010814-015924
762 Steinberg, D. K., Van Mooy, B. A. S., Buesseler, K. O., Boyd, P. W., Kobari, T., & Karl, D.
763 M. (2008). Bacterial vs. zooplankton control of sinking particle flux in the ocean's
764 twilight zone. *Limnology and Oceanography*, *53*(4), 1327–1338.
765 https://doi.org/10.4319/lo.2008.53.4.1327
766 Stramski, D., Boss, E., Bogucki, D., & Voss, K. J. (2004). The role of seawater constituents in
767 light backscattering in the ocean. *Progress in Oceanography*, *61*(1), 27–56.
768 https://doi.org/10.1016/j.pocean.2004.07.001
769 Stramski, D., Bricaud, A., & Morel, A. (2001). Modeling the inherent optical properties of the
770 ocean based on the detailed composition of the planktonic community. *Applied Optics*,
771 *40*(18), 2929–2945. https://doi.org/10.1364/AO.40.002929
772 Stramski, D., & Kiefer, D. A. (1991). Light scattering by microorganisms in the open ocean.
773 *Progress in Oceanography*, *28*(4), 343–383. https://doi.org/10.1016/0079-
774 6611(91)90032-H
775 Taylor, J. R., & Ferrari, R. (2011). Shutdown of turbulent convection as a new criterion for
776 the onset of spring phytoplankton blooms. *Limnol. Oceanogr.*, *56(6)*, 2293–2307.
777 Thomas, L. N., & Lee, C. M. (2005). Intensification of ocean fronts. *Bulletin of the American*
778 *Meteorological Society*, *86*(6), 783. https://doi.org/10.1175/JPO2737.1
779 Turner, J. T. (2002). Zooplankton fecal pellets, marine snow and sinking phytoplankton
780 blooms. *Aquatic Microbial Ecology*, *27*(1), 57–102. https://doi.org/10.3354/ame027057
781 Turner, J. T. (2004). The Importance of Small Pelagic Planktonic Copepods and Their Role in
782 Pelagic Marine Food Webs. *Zoological Studies*, *43*(2), 255–266.
783 Turner, J. T. (2015). Zooplankton fecal pellets, marine snow, phytodetritus and the ocean's
784 biological pump. *Progress in Oceanography*, *130*, 205–248.
785 https://doi.org/10.1016/j.pocean.2014.08.005
786 Turner, J. T., Levinsen, H., Nielsen, T. G., & Hansen, B. W. (2001). Zooplankton feeding
787 ecology: Grazing on phytoplankton and predation on protozoans by copepod and
788 barnacle nauplii in Disko Bay, West Greenland. *Marine Ecology Progress Series*. Inter-
789 Research Science Center. https://doi.org/10.3354/meps221209
790 Villa-Alfageme, M., de Soto, F. C., Ceballos-Romero, E., Giering, S., Le Moigne, F. A. C.,
791 Henson, S., & Sanders, R. J. (2016). Geographical, seasonal and depth variation in
792 sinking particle speeds in the North Atlantic. *Manuscript Submitted for Publication*.
793 https://doi.org/10.1002/2016GL069233
794 Visser, A. W., Saito, H., Saiz, E., & Kiørboe, T. (2001). Observations of copepod feeding and
795 vertical distribution under natural turbulent conditions in the North Sea. *Marine Biology*,
796 *138*(5), 1011–1019. https://doi.org/10.1007/s002270000520
797 Wang, W., & Huang, R. X. (2004). Wind energy input to the surface waves. *Journal of*
798 *Physical Oceanography*, *34*(5), 1276–1280. https://doi.org/10.1175/1520-
799 0485(2004)034<1276:WEITTS>2.0.CO;2
800 Wong, A., Keeley, R., Carval, T., & Argo Data Management Team. (2015). Argo Quality
801 Control Manual For CTD and Trajectory Data, (December), 1–56. Retrieved from
802 http://archimer.ifremer.fr/doc/00228/33951/
803 Woods, J. D. (1980). Diurnal and seasonal variation of convection in the wind-mixed layer of
804 the ocean. *Quarterly Journal of the Royal Meteorological Society*, *106*(449), 379–394.
805 https://doi.org/10.1002/qj.49710644902
806 Woods, J. D., & Onken, R. (1982). Diurnal variation and primary production in the ocean
807 preliminary results of a Lagrangian ensemble model. *Journal of Plankton Research*, *4*(3),
808 735–756. https://doi.org/10.1093/plankt/4.3.735
809 Xing, X., Briggs, N., Boss, E., & Claustre, H. (2018). Improved correction for non-

photochemical quenching of in situ chlorophyll fluorescence based on a synchronous irradiance profile. *Opt. Express*, *26*(19), 24734–24751. https://doi.org/10.1364/OE.26.024734

Xing, X., Claustre, H., Boss, E., Roesler, C., Organelli, E., Poteau, A., … D'Ortenzio, F. (2017). Correction of profiles of in-situ chlorophyll fluorometry for the contribution of fluorescence originating from non-algal matter. *Limnology and Oceanography: Methods*, *15*(1), 80–93. https://doi.org/10.1002/lom3.10144

Xing, X., Morel, A., Claustre, H., Antoine, D., D'Ortenzio, F., Poteau, A., … Hu, C. (2011). Combined processing and mutual interpretation of radiometry and fluorimetry from autonomous profiling Bio Argo floats: Chlorophyll a retrieval. *Journal of Geophysical Research-Oceans*, *116*(C6), C06020. https://doi.org/10.1029/2010JC006899

Zawada, D. G., Zaneveld, J. R. V., Boss, E., Gardner, W. D., Richardson, M. J., & Mishonov, A. V. (2005). A comparison of hydrographically and optically derived mixed layer depths. *Journal of Geophysical Research*, *110*(C11), C11001. https://doi.org/10.1029/2004JC002417

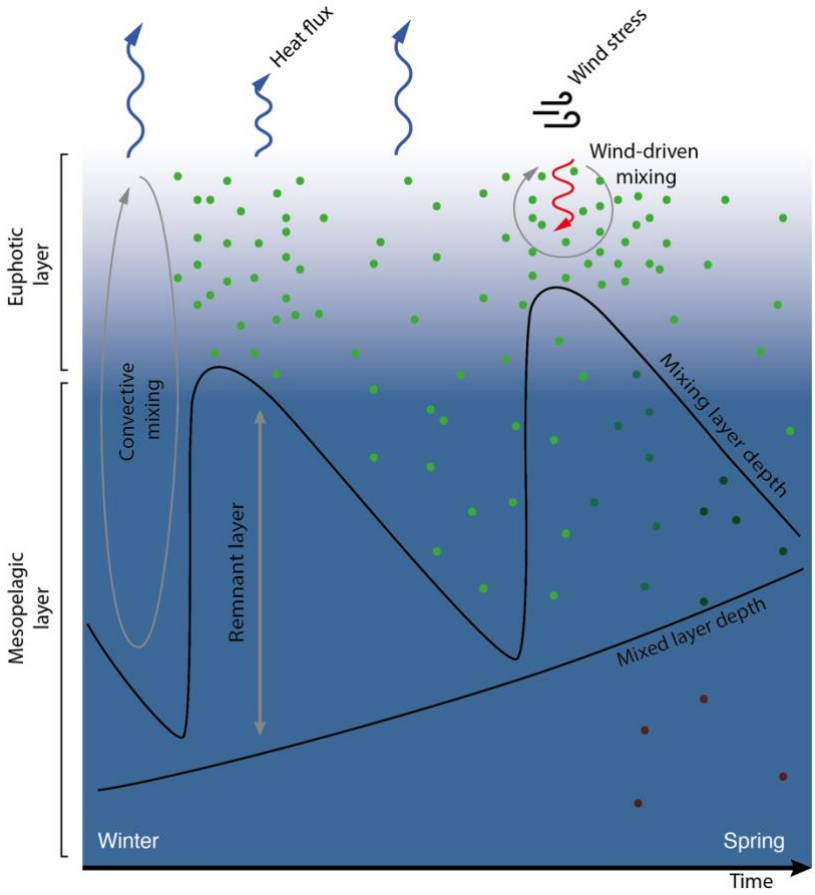

Figure 1. Schematic of the functioning of the intra-seasonal mixed layer pump.

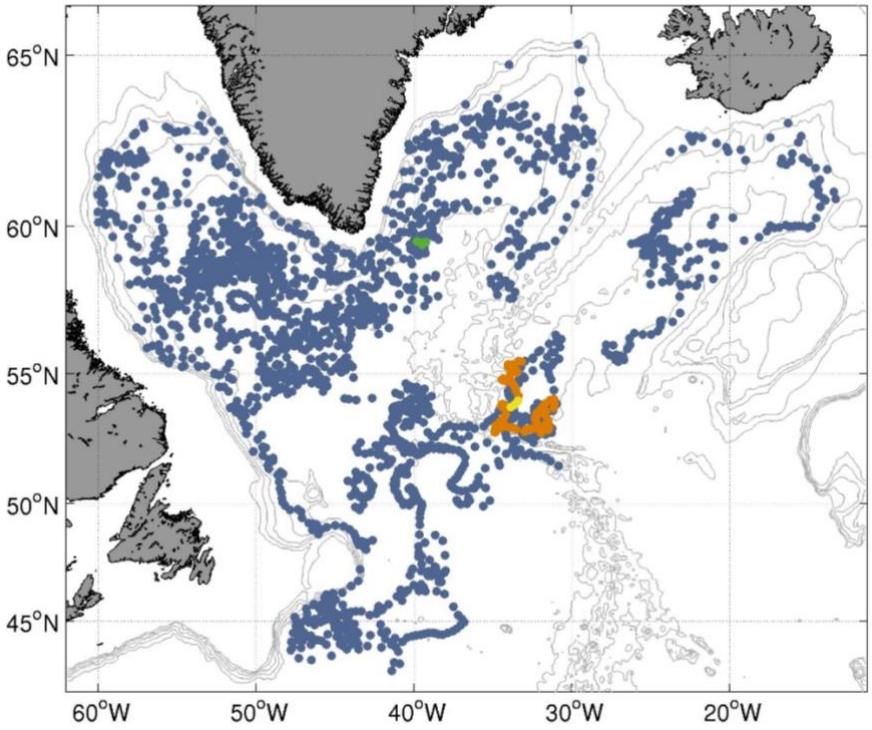

Figure 2. Location of the BGC-Argo float profiles in the subpolar North Atlantic Ocean during 2014-2016. Orange dots indicate the location of float 6901516 trajectory (January-December 2014) shown in Fig. 5. Yellow and green dots indicate the location of profiles shown in Fig. 7a and b respectively.

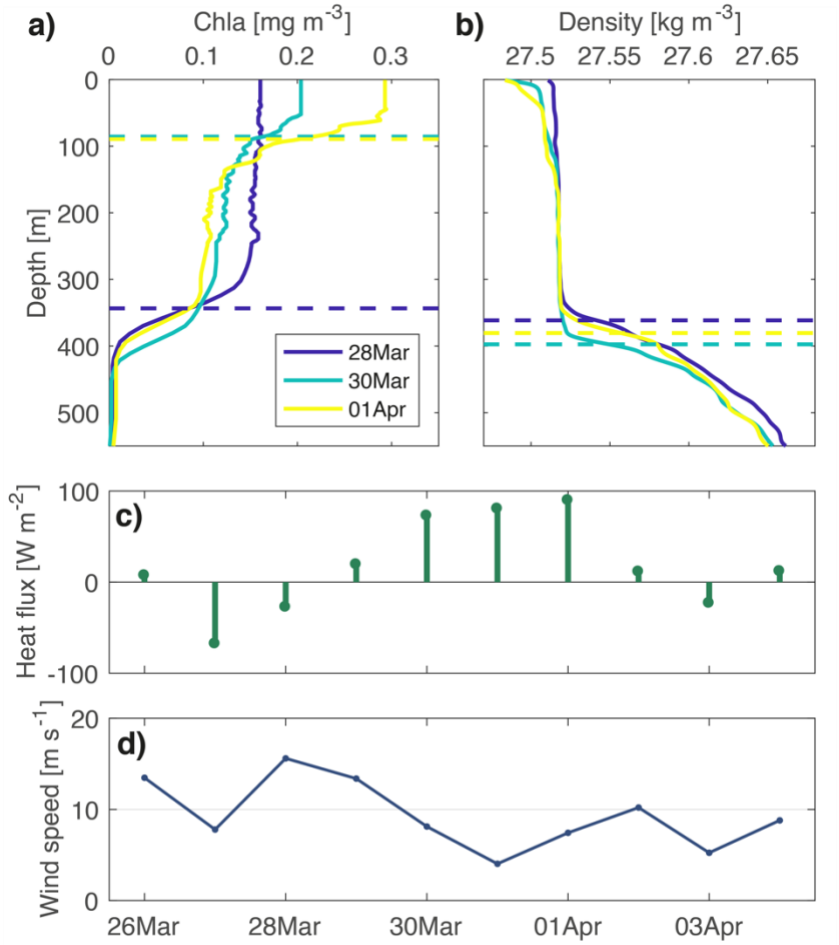

Figure 3. Three BGC-Argo float profiles along the float 6901516 trajectory (yellow dots in Fig. 2) sampled in the same water mass (see Fig. 7a) from March 28th to April 1st 2014. **a)** Chla profiles and **b)** density profiles with 2-day intervals. Horizontal dashed lines mark the depth of the maximum Chla gradient (MLD_{bio}) in **a)** and maximum density gradient (MLD_{dens}) in **b)**. Constant Chla in the upper layer in **a)** is due to NPQ correction. **c)** Daily net heat flux and **d)** wind speed along the float trajectory.

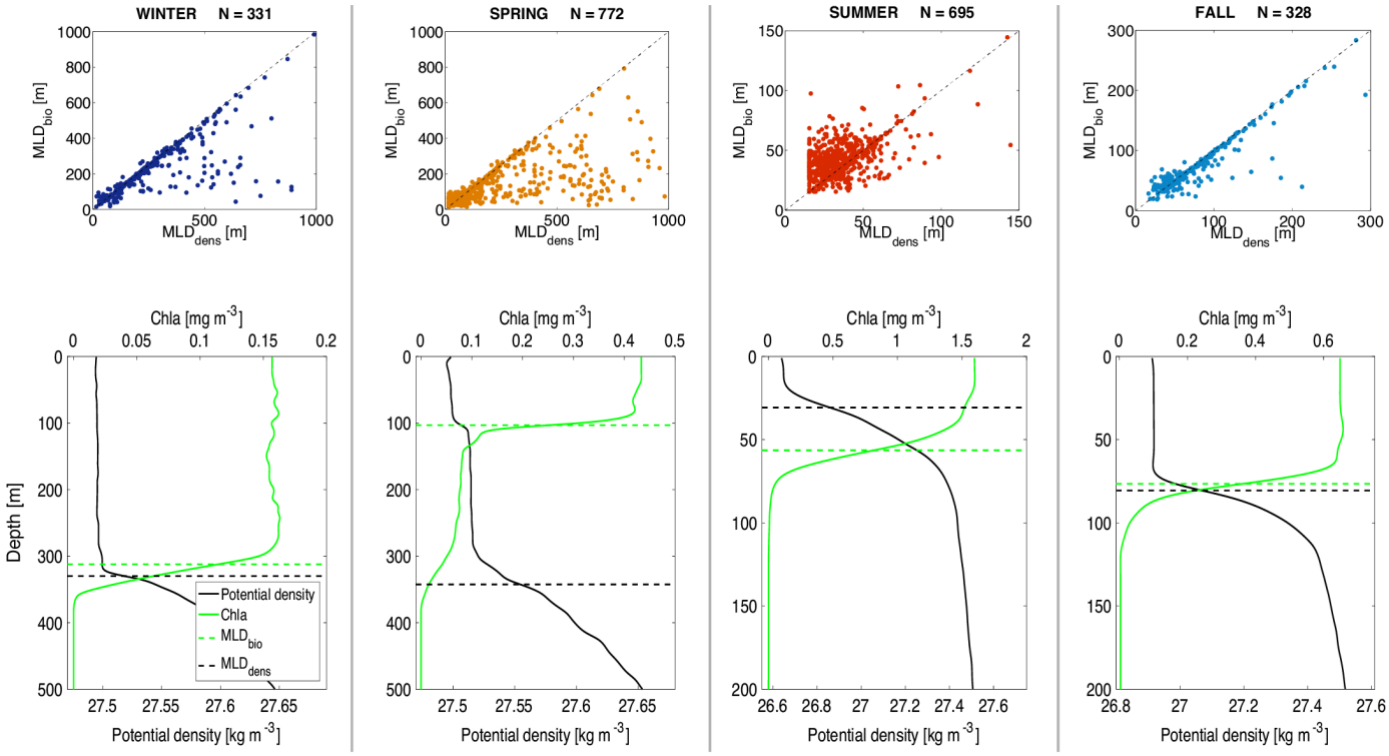

841

Figure 4. Seasonal difference between MLD_{bio} and MLD_{dens} for all the profiles shown in Fig. 2 (top) and examples of Chla and density profiles by season (bottom). Horizontal dashed black and green lines mark MLD_{dens} and MLD_{bio} respectively.

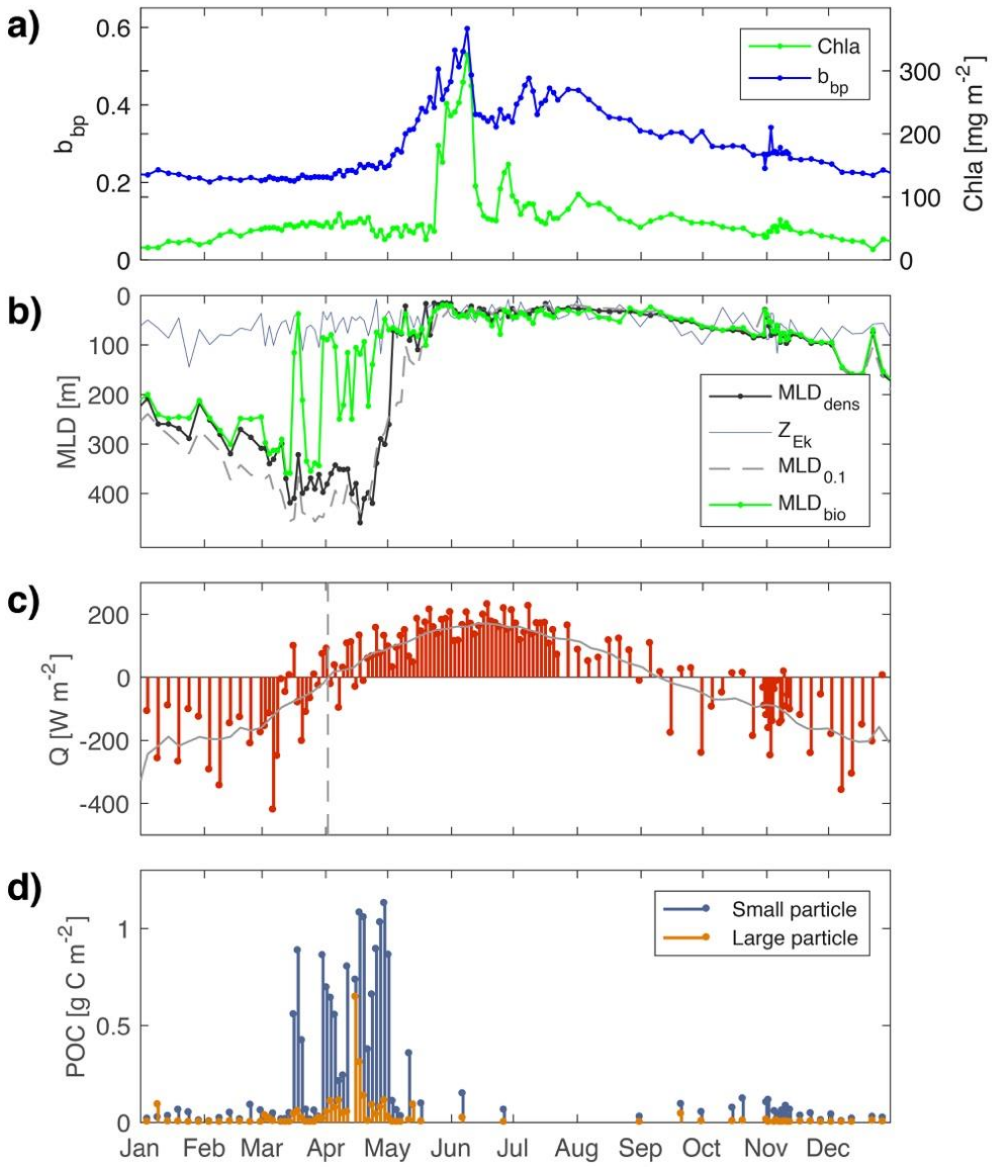

Figure 5. Impact of the mixing layer dynamics on POC export. **a)** Chla and b_{bp} integrated over 0-1,000 m depth (integrated b_{bp} is dimensionless), **b)** MLD_{dens}, MLD_{bio}, $MLD_{0.1}$ estimated with a density threshold of 0.1 kg.m^{-3}, and the Ekman length scale Z_{Ek}, **c)** Daily-averaged net heat flux (Q) and **d)** POC stocks trapped in the remnant layer along the float 6901516 trajectory (January-December 2014). Continuous grey line and vertical dashed grey line in c) show 30-day smoothed net heat flux and the date of zero-crossing net heat flux respectively.

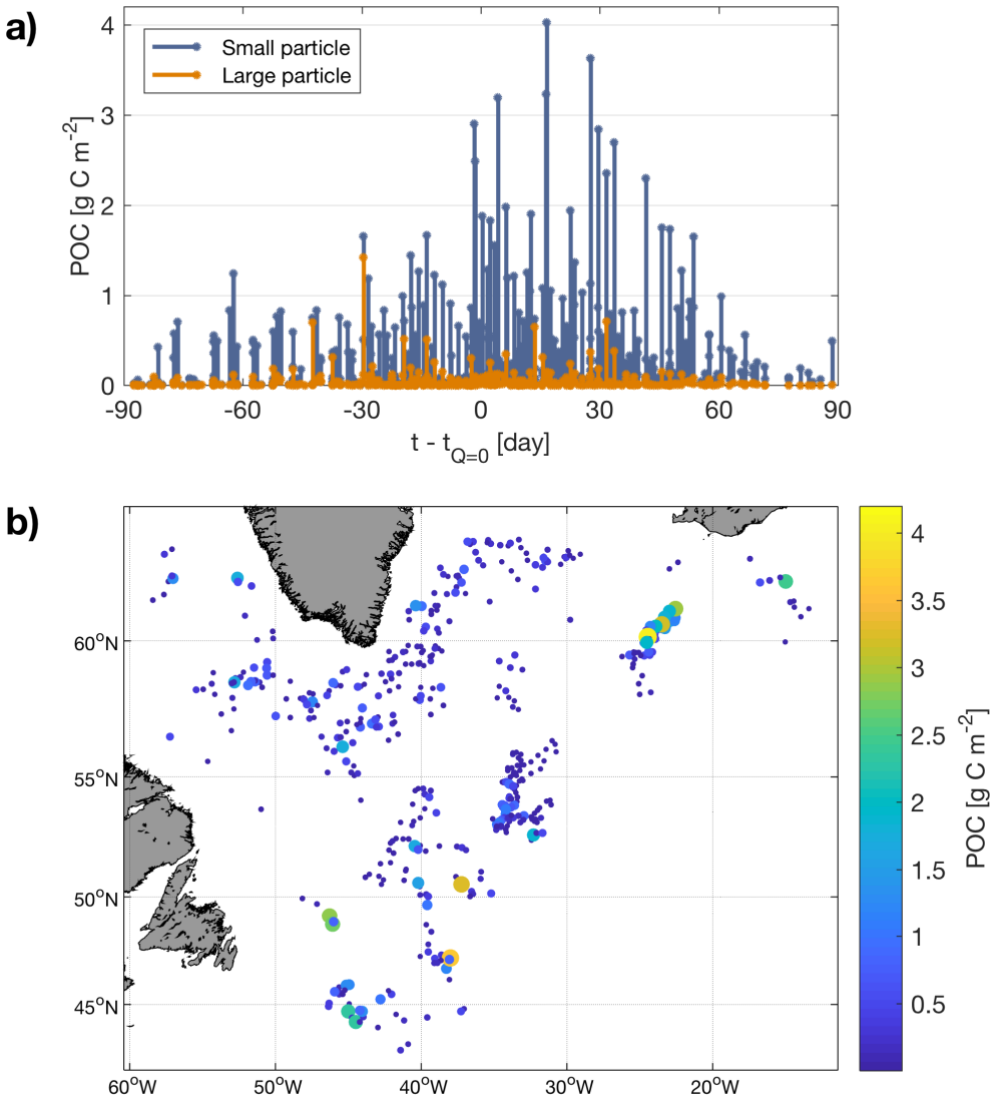

Figure 6. **a)** POC stock transferred to the mesopelagic by mixed layer pump events measured by the floats over the whole subpolar region. The time axis refers to the day of observation relative to the day where the sign of heat flux changes from negative to positive (see Fig. 5c). **b)** Location of profiles presenting ML pump signature. Color and dot size denote the stock of small particles trapped in the remnant layer.

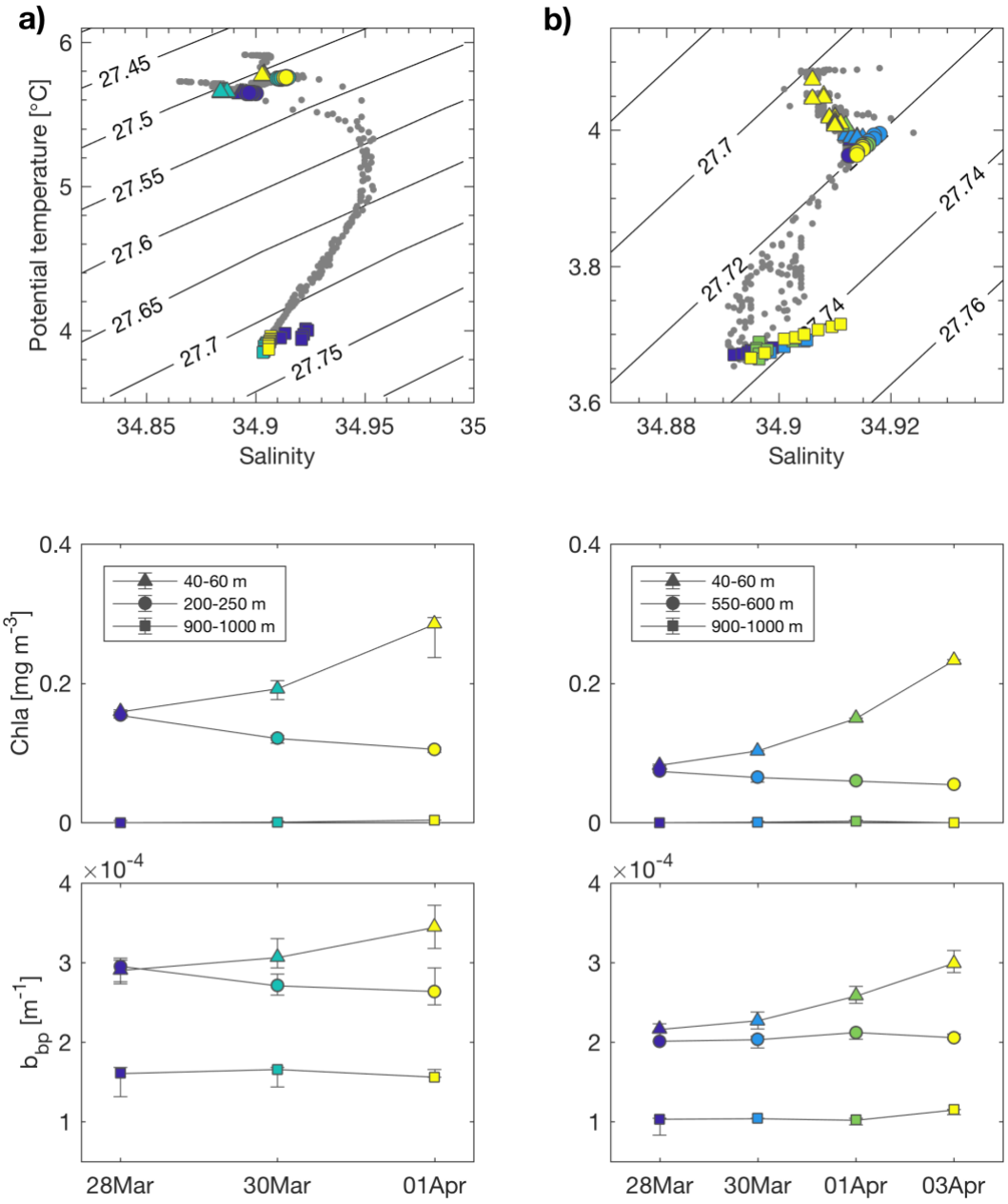

Figure 7. A quasi-Lagrangian approach to the ML pump. BGC-Argo float profiles along 2 sections of **a)** float 6901516 and **b)** float 6901480 acquired in 2014 (see location in Fig. 2). Top panels show potential temperature and salinity diagram for each profile of the 2 sections. Bottom panels show time evolution of mean Chla and b_{bp} from each profile over 3 different layers: surface (triangle), remnant (filled circle) and deep layer (square). Vertical error bars indicate the range of data points within each layer. Color of the symbols differentiates each profile.

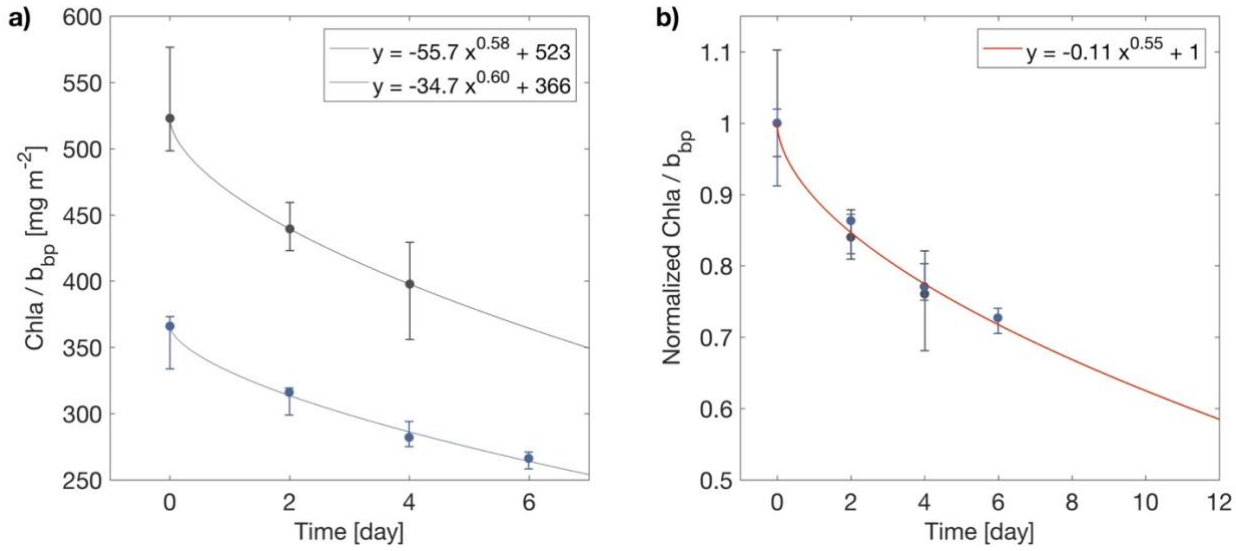

Figure 8. Time evolution of the Chla to b_{bp} ratio in the remnant layer. **a)** Absolute and **b)** normalized (by the maximum value) Chla to b_{bp} ratio for sections of float 6901516 (black line) and 6901480 (blue line) shown in Fig. 2 and 7. The red line represents the best-fit power law function for both float sections. The vertical error bars indicate the range of data points within the remnant layer.

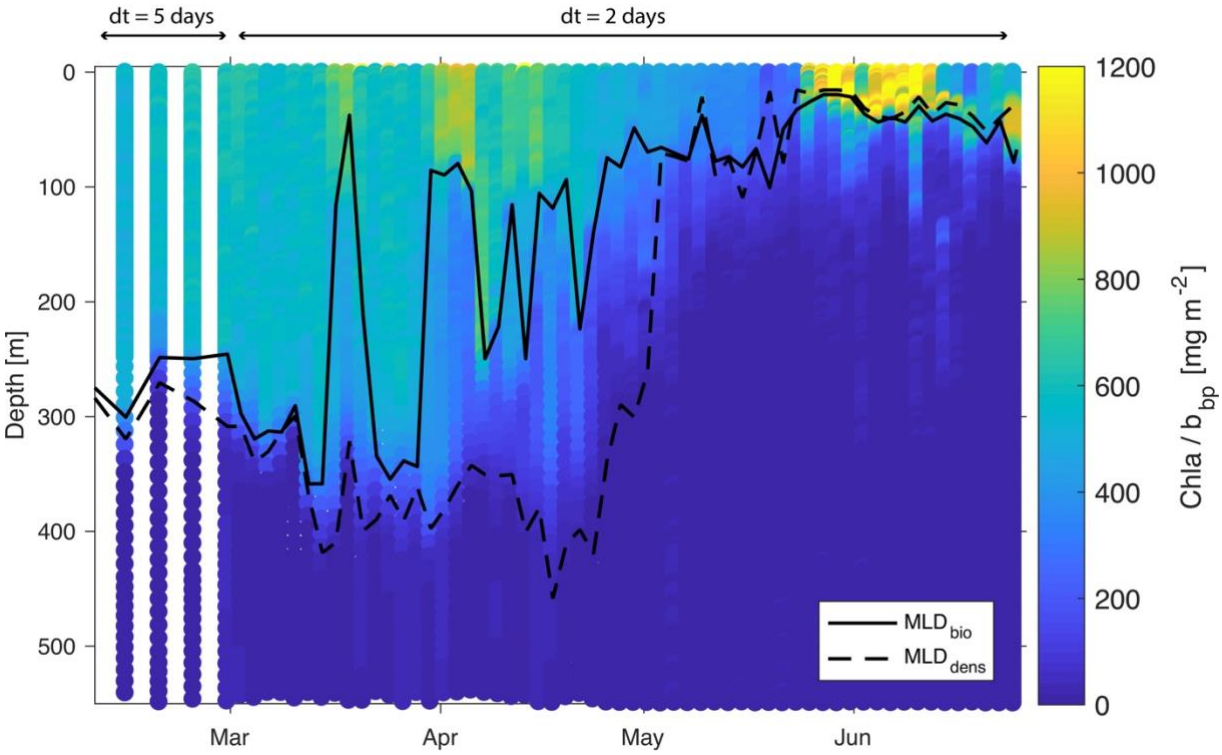

Figure 9. Time series of Chla to b_{bp} ratio at each depth along the float trajectory 6901516 (February-July 2014). Solid black line and dashed black line represent MLD_{bio} and MLD_{dens} respectively. Time interval (dt) between successive profiles is indicated at the top of the panel.

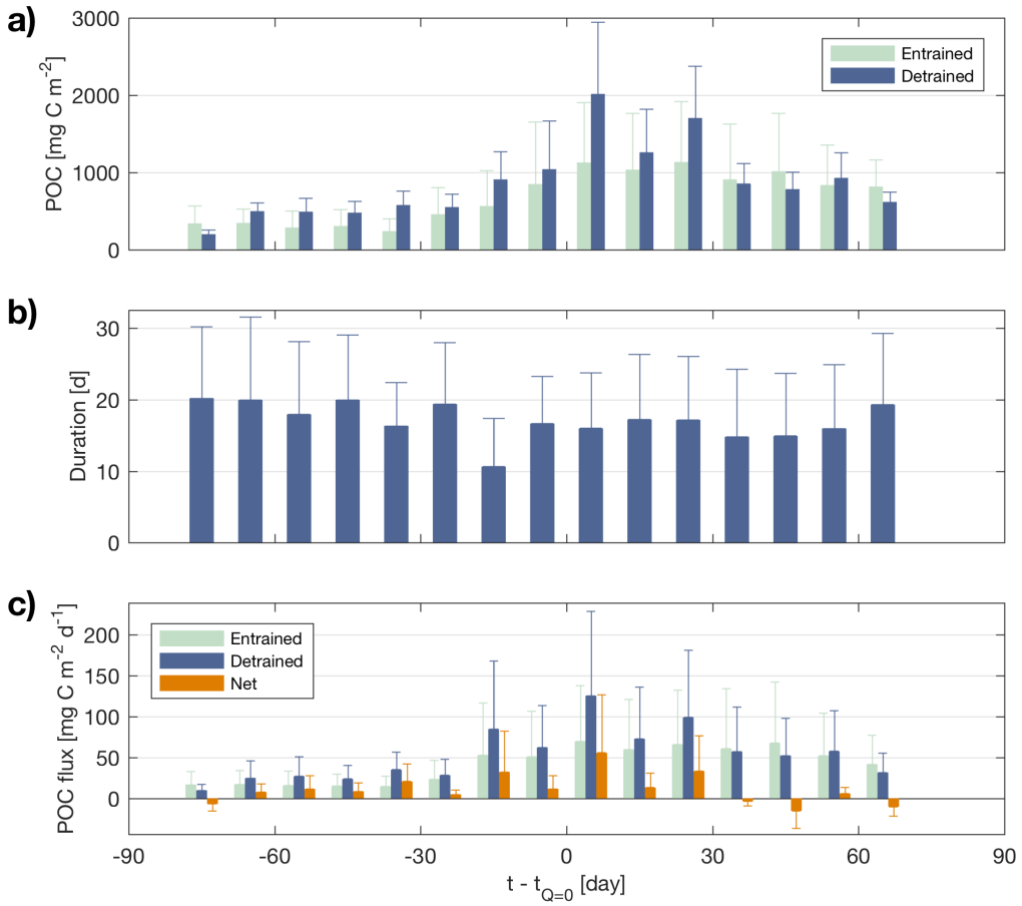

Figure 10. a) POC stock entrained and detrained from the mixing layer, as estimated from initial conditions, b) duration of ML pump events (i.e. $2 < \Delta t >$) and c) Entrained, detrained and net ML pump-driven POC fluxes averaged over 10-day time periods in the whole subpolar North Atlantic Ocean. The length of error bars represents the average standard deviation of initial conditions associated to each ML pump signature detected within a 10-day time period. The time axis refers to the day of observation relative to the day where the sign of heat flux changes from negative to positive (see Fig. 5c).